

Glycosylation-Targeting Aptamer for the Feasible Construction of a Dual Aptamer-Based Plasmonic Immunosandwich Assay in Cancer Diagnostics

Junyang Chen, Pengfei Ma, Jiayu Xu, Mingxi Zang, and Wei Li*

Cite This: *Anal. Chem.* 2025, 97, 203–211

Read Online

ACCESS |



Metrics & More

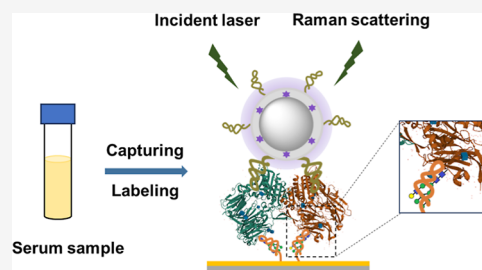


Article Recommendations



Supporting Information

ABSTRACT: Fibroblast activation protein (FAP) is an important antigen in the tumor microenvironment, which plays a crucial role in promoting extracellular matrix remodeling and tumor cell metastasis. A circulating form of soluble FAP has also been identified in the serum, becoming a biomarker for pan-cancer diagnosis and prognosis. However, the current peptide substrate-based enzymatic activity detection or antibody-dependent detection methods have been hindered by insufficient selectivity and complex operations, so it is valuable to develop effective nucleic acid aptamers as FAP affinity ligands. In order to deeply explore the biomimetic recognition technology, this study proposed an elaborate aptamer screening strategy for targeting the protein characteristic structure. Taking the glycosylation of the FAP protein as a target, four FAP-specific aptamers with high performance were successfully generated. Further, using the champion aptamer as a recognition tool and combining it with ultrasensitive detection technology-surface enhanced Raman scattering (SERS), a novel dual aptamer-based sandwich sensor was constructed for the rapid determination of FAP. Due to the dual-specific recognition of the orthogonal aptamer pair, the sandwich method obviously improved the selectivity to FAP protein, with a maximum cross-reactivity of less than 8% and a quantitation limit of 100 pg/mL. It was conveniently applied in high-sensitive and high-selective detection of serum FAP in cancer patient samples. Therefore, the research of this study not only opens new access for the selection of antiglycan aptamers but also boosts the application of the FAP aptamer as a recognition tool in cancer diagnostics.



Malignant tumors are the main cause of global morbidity and mortality and have become a major public health issue threatening human life.¹ In addition to the uncontrolled proliferation of malignant cells, the occurrence and progression of tumors are closely related to the complex components in the tumor microenvironment. As a result, strategies focused on biomarkers of tumor cells sometimes are inadequate for significant patient outcomes, even leading to delayed diagnosis, incomplete treatment, and poor prognosis.^{2–4} Fibroblast activation protein (FAP) has been proven to be a unique marker in the tumor microenvironment because of its overexpression on the reactive cancer-associated fibroblasts but absent from quiescent fibroblasts. As a transmembrane serine protease, FAP facilitates remodeling of the extracellular matrix and thereby promotes tumor growth, invasion, metastasis, and angiogenesis.⁵ Thus, it has drawn emerging interest in clinical translation, such as pan-tumoral imaging, cancer diagnostics, and therapeutics.

Despite numerous studies investigating FAP as a putative biomarker for several types of cancer and their corresponding prognosis, effective methodologies for FAP quantification are still in great demand. FAP is mostly present as a homodimeric transmembrane glycoprotein, and the extracellular region contains the entire catalytic domain and N-glycosylation

modification.^{6,7} Also, a soluble form of FAP, which shed from the plasma membrane, has been found in the tissue fluid and blood.⁸ Due to a similar structure to the family member dipeptidase IV (DPP4), FAP processes identical dipeptidyl peptidase activity, while it has an extra endopeptidase activity.⁹ Hence, endopeptidase activity is the main distinguishing feature for FAP-specific detection methods via colorimetric or fluorescent peptide substrates.^{10,11} Besides, there are some other strategies to quantify FAP levels, including genotypic tests through reverse transcription-polymerase chain reaction in the mRNA expression level¹² and protein measurement by antibody-based immunohistochemistry,¹³ Western blotting,¹⁴ and liquid chromatography/mass spectroscopy (LC/MS).¹⁵ Nevertheless, those genotypic and protein detection methods are of high cost and time-consuming and require highly skilled personnel for credible results, which immensely limit diverse applicability in actual samples. Although enzymatic activity

Received: July 20, 2024

Revised: December 14, 2024

Accepted: December 16, 2024

Published: December 23, 2024



detection methods based on optical analysis demonstrate fast response and economical cost, they are always hindered by insufficient selectivity and poor immunity to interference.¹⁶ Therefore, it is of crucial importance to establish a new analytical method with high sensitivity and selectivity for accurate FAP detection.

Nucleic acid aptamers are one of the most representative synthetic affinity ligands, with a highly favorable recognition performance comparable to artificial antibodies. They are short, single-stranded (ss) DNA or RNA oligonucleotides that specifically bind various species from metal ions, small molecules, carbohydrates, proteins, and cells to viruses.^{17,18} Aptamers are usually obtained through the process of systematic evolution of ligands by exponential enrichment (SELEX)^{19–22} and exhibit important applications in sensing, imaging, and as a therapeutic drug.^{23,24} Due to their characteristics of small size, easy chemical modification, and cost effectivity, they provide a useful tool to construct aptamer-based sandwich assays for the determination of trace proteins in biological samples.^{25,26} Through the combination with the sensitive analytical method or techniques such as fluorescence, electrochemical detection, and chemiluminescence, the detection performance has achieved apparent improvement.^{27–29} Particularly, surface-enhanced Raman scattering (SERS) is attracting increasing attention because of its additional strengths over conventional detection schemes.^{30,31} As an ultrasensitive detection technique, SERS offers high sensitivity, rapid readout speed, and good anti-interference ability and allows for direct testing without complex pretreatment. By virtue of the plasmonic coupling effect between a gold-coated substrate and silver-cored SERS labeling nanotags, an appealing approach termed as the plasmonic immunosandwich assay (PISA) has demonstrated additional signal enhancement in real-world determination.^{32–36} Although orthogonal dual molecularly imprinted polymer-based PISA could greatly ensure the detection specificity toward glycoprotein disease biomarkers,³² it often requires characteristic preparation of polymers. Hence, the exploration of a possible fashion for dual aptamer-based PISA is a kind of viable strategy in sensitive FAP detection.

Notably, a special challenge to construct an ideal dual aptamer-based sandwich assay is the appropriate aptamer pairs that bind the target at two different sites. Even though some attempts, such as target immobilization-free SELEX, machine prediction, and secondary aptamer confirmation, have been made to obtain aptamer pairs,^{37–39} it has still remained a significant lack of convenient approaches. Delightingly, aptamers targeting protein-specific glycosylation are becoming attractive ligands owing to their promise in the improvement of clinical practice for tumor biomarkers.^{40–44} Different from the large number of protein-binding aptamers, glycan-binding aptamers possess unique specificity toward glycan domains of glycoproteins but random orientations or uncertain sites. This would greatly facilitate the choice of orthogonal aptamer pairs for the construction of sandwich assays. However, since the limited options regarding noncovalent binding interactions between sugars and oligonucleotides,⁴⁵ a wider development potential has been stuck in the dilemma of inadequate aptamers against glycans.

Herein, we report a new approach for feasibly constructing an orthogonal dual aptamer (oda)-based PISA for accurately determining FAP in complex samples. Aiming at the characteristic structure of FAP protein, glycosylation, we first

proposed an elaborate SELEX strategy for the efficient selection of glycan-binding aptamers. Via implementing strict glycan-guided screening processes, which alternately introduce glycoprotein FAP and artificial deglycosylated FAP in steps, four aptamers with satisfactory performances were successfully obtained. Further, a high-performance oda-based biosensor was established for rapid and sensitive detection of FAP by utilizing a glycan-targeting aptamer along with a protein-binding aptamer in PISA. We also demonstrated the facile FAP determination in serum samples, which allowed for differentiation of the cancer patient from the healthy individual. Compared with antibody-based immunoassays, this method has a fast and sensitive response, as well as a wide detection range, thus obviating tedious sample pretests. Therefore, this study provides a new FAP-specific quantitative method with high sensitivity and selectivity, and it holds strong practical applications for clinical diagnosis.

EXPERIMENTAL SECTION

SELEX Procedure. One nmol of the initial ssDNA library was dissolved in 100 μL of binding buffer and then heated at 95 $^{\circ}\text{C}$ for 10 min before being cooled on ice for 10 min. Two mg of FAP-immobilized magnetic nanoparticles (MNPs) were added and incubated at room temperature for 2 h on a rotary shaker. Through magnetic separation, the supernatant solution was discarded, and then the MNPs-FAP-ssDNA complexes were washed with washing buffer twice. The bound ssDNA was eluted by heating at 95 $^{\circ}\text{C}$ for 15 min with 100 μL of binding buffer. After magnetic separation, the elution was collected and was used as a template for polymerase chain reaction (PCR) amplification. After isolation by streptavidin-coated beads, the ssDNA pool was collected and used later for the next round of selection. Three rounds of positive selection later, negative and counter selection steps were respectively introduced to improve the selectivity of aptamers. Specifically, the evolved pool was incubated with the negative target (BSA-immobilized MNPs) or counter target (deglycosylated FAP-immobilized MNPs), prior to incubating with FAP-immobilized MNPs. The incubation time and washing strength were gradually varied, and the detailed selection conditions are listed in Table S2.

Preparation of the Aptamer-Modified Array and Raman Nanotags. The process of the aptamer-modified array was composed of two steps: the preparation of (1) Au-coated glass slides and (2) a Seq2T aptamer-modified array. Aptamer-modified Raman nanotags were also prepared with two steps, including (1) synthesis of silver nanoparticles (AgNPs) and (2) preparation of A1 aptamer-modified Raman nanotags as the route in Figure S13A. The experimental details are given in the Supporting Information.

Plasmonic Immunosandwich Assay. The procedure of the PISA included three steps: (1) target capturing, (2) labeling with Raman nanotags, and (3) detection. For the capturing, 5 μL aliquots of FAP standard solutions or serum samples were added onto each spot of the Seq2T aptamer-modified arrays, allowed to incubate for 20 min in a humidity chamber, and then washed with 10 mM PBS buffer (pH 7.4) three times to remove unwanted species. For the labeling, the arrays were incubated with 5 μL of A1 aptamer-modified Raman nanotags for 5 min and washed with 10 mM PBS buffer (pH 7.4) three times to remove excess nanotags. After being dried at room temperature, the arrays were subjected to a

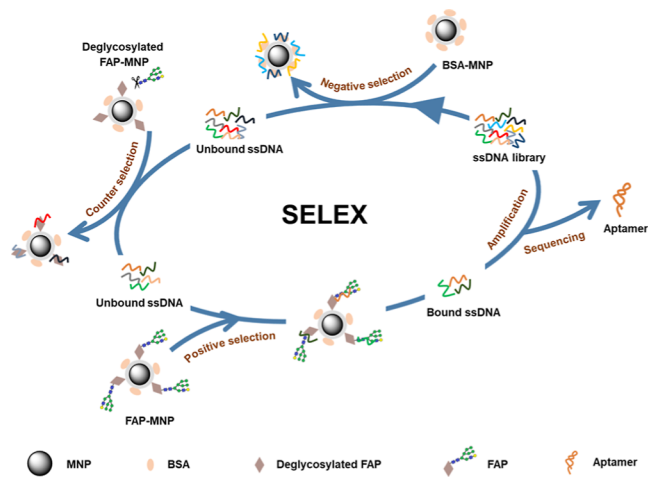
Raman spectrograph for the signal readout in the detection step.

RESULTS AND DISCUSSION

Aptamer Selection Strategy. A magnetic-bead-based selection approach was used in this work. The synthesis route and morphology of MNPs are shown in Figure S1A–D, giving an average diameter of about 100–150 nm. A photograph also demonstrated their dispersion and magnetic separation (Figure S1E). Fourier transform infrared characterization confirmed the successful modification process of MNPs (Figure S1F). Due to the advantages of small diameter, large surface area, good stability, and less sedimentation, these MNPs were excellent immobilized carriers for other molecules. Protein targets were immobilized by cross-linking with glutaraldehyde onto MNPs. As shown in Figure S1G, the amounts of FAP protein in solution were significantly reduced after incubation, and little was found in the buffer after washing, demonstrating the proteins were successfully immobilized on the surface of MNPs. The DNA nonspecific adsorption ratios on different MNPs were also observed in Figure S2, indicating that glutaraldehyde-functionalized MNPs were beneficial for later aptamer selection.

Our SELEX process is illustrated in Scheme 1; FAP-immobilized MNPs were introduced in positive selection, and

Scheme 1. Schematic of the SELEX Process of FAP Glycan-Targeted Aptamers



unreacted functional groups on the surface of beads were blocked with bovine serum albumin (BSA). After a sufficient amount of ssDNA was obtained by three rounds of positive selection, negative selection with BSA-immobilized MNPs was introduced to remove aptamers that recognize the solid support, while counterselection with deglycosylated FAP (de-FAP)-immobilized MNPs allowed for glycan-oriented screening. Through the combination of the positive target of FAP glycoprotein and the counter target of deglycosylated FAP, aptamers against the glycan moiety of FAP could be directly enriched during the selection process. Although a few works attempted to incorporate similar counter-selection with the recombinant deglycosylated protein for glycan-guided aptamer selection,^{40,41} the deglycosylated form by the enzymatic reaction is obviously a more general protocol to get this type of receptor against *N*-glycoproteins. The sequence of the initial library for the selection is given in Table S1, while the detailed

selection conditions are specified in Table S2. At each round of selection, the pressure was gradually enhanced by varying the incubation time and washing strength.

The enrichment level of specific ssDNA in SELEX rounds was monitored. The eluate of each round was amplified by symmetry PCR using a FAM-forward primer and biotin-reverse primer, and the FAM-ssDNA pool was generated by magnetic separation with streptavidin-coated beads. The quality of the ssDNA obtained from PCR products was checked by agarose gel electrophoresis (Figure S3A). There is a clear and well-defined band that corresponds to ssDNA, indicating the successful separation of ssDNA sequences. The binding affinity of each round ssDNA pool toward a positive target was evaluated by a fluorescence method. As shown in Figure 1A, the bound fraction of ssDNA toward the positive

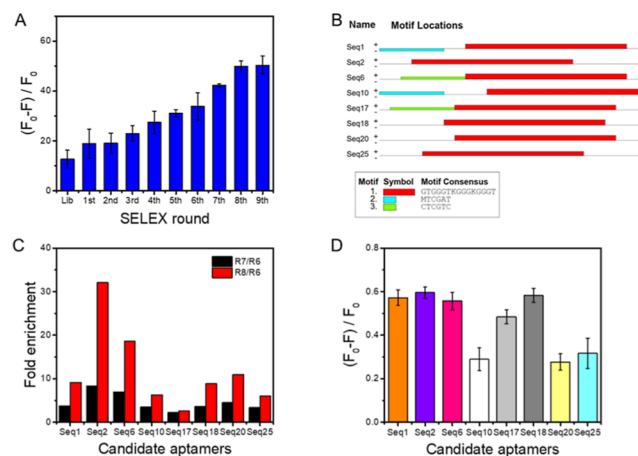


Figure 1. (A) Evolution progress of specific ssDNA. (B) Visualization of the most prevalent motifs represented in the selected aptamer candidates. All motifs were found within central core sequences without involvement of constant prime sequences. (C) Enrichment of candidate aptamer sequences between rounds of selection. Fold enrichment is calculated by dividing the percentage of the sequence from round 7 (R7) or round 8 (R8) by the percentage of the sequence from round 6 (R6). (D) Binding affinity of candidate aptamers (equal aptamer concentrations at 200 nM). Error bars represent standard deviations for three parallel measurements.

target moderately rose as the screening round grew, and a significant increase appeared with the addition of negative and counter steps after three rounds, suggesting improved selection pressure and efficiency. The binding ratio to the positive target reached a plateau at the eighth round; subsequently, the specificities of the last two ssDNA pools from the eighth-ninth round were confirmed in Figure S3B. These pools showed similarly high affinity to the positive selection target (FAP) with limited binding to the counter and negative targets (de-FAP and BSA). All the results suggest successful enrichment of specific sequences, and the selection reached saturation at the eighth round. The final aptamer pool products from round 8 (R8) and the previous two rounds (R6 and R7) were sent for next-generation sequencing.

Characterization of the Selected Aptamers. The 25 most predominant sequences in the final aptamer pool (R8) were analyzed by sequence alignment, and their evolutionary relationships also were evaluated through the phylogenetic tree analysis (Figure S4). Considering the abundance ranking and family distribution of the sequences, eight representative aptamer sequences, Seq1, 2, 6, 10, 17, 18, 20, and 25 from

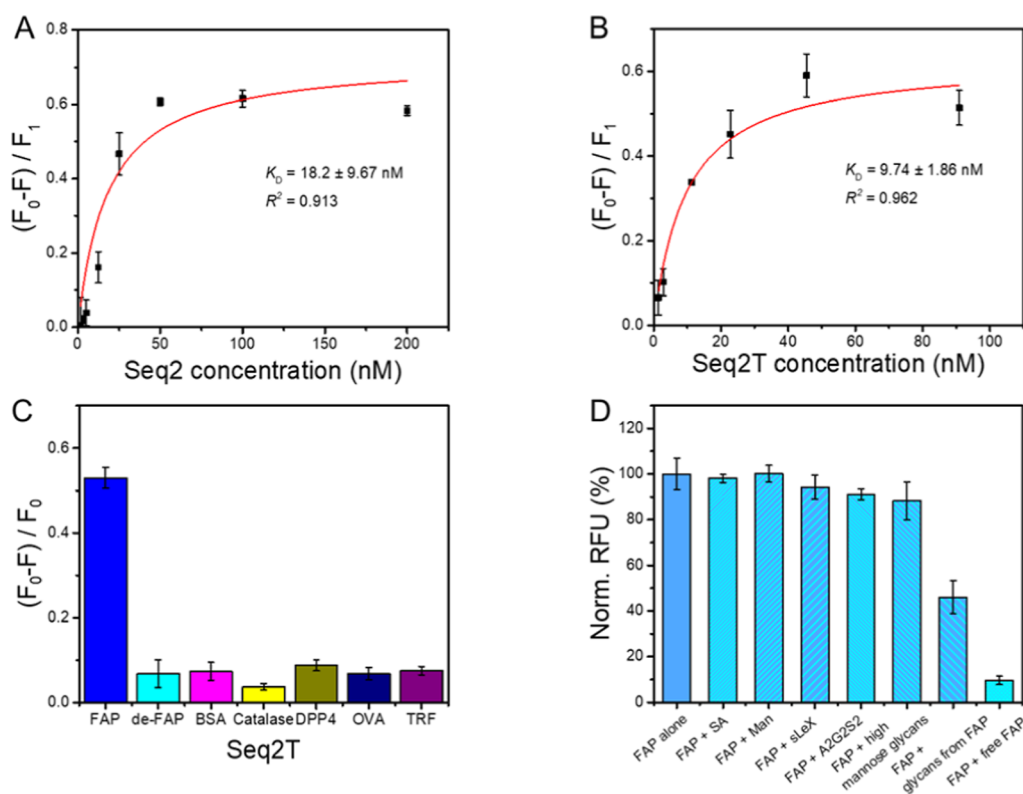


Figure 2. Property characterization of champion aptamers. The binding curves and dissociation constant determination of the candidate aptamers (A) Seq2 and (B) Seq2T. (C) Specificity test of Seq2T. (D) Competitive binding assays for Seq2T and FAP alone or with free sialic acid (SA), Man, sialyl lewis X (sLeX), A2G2S2 glycan from TRF, high mannose glycans from RNase B, glycans from FAP, and FAP. The y-axis shows relative fluorescence normalized to the FAP-only control. The error bars represent the standard deviation for three parallel experiments.

three clusters, were selected as candidates for functional validation. The possible functional structural domains (motifs) on the aptamers were predicted by the Multiple Em for the Motif Elicitation (MEME) suite (<https://meme-suite.org/>). It was found that the eight candidate aptamers all contained a conserved motif consisting of 15 bases (motif 1, Figure 1B and Table S3), while motif 2 (seqs 1 and 10) and motif 3 (seqs 6 and 17) only appeared in several sequences. The predicted secondary structures corresponding to these aptamers showed similar features (Figure S5), and their minimum free energy (dG) values are listed in Table S4. The enrichment progression from SELEX rounds 6 to 8 (R6 to R8) was also calculated (Figure 1C). The aptamer of Seq2 exhibited the strongest fold enrichment ($R8/R6 = 32.11$ and $R7/R6 = 8.37$), and Seq17 was the weakest ($R8/R6 = 2.66$), with Seq1, 6, 10, 18, 20, and 25 between them. For functional validation, candidate aptamers were synthesized and labeled with a FAM fluorescent reporter at the 5' end. The affinities of these aptamers toward FAP protein were preliminarily evaluated in Figure 1D. Among them, aptamers of Seq1, 2, 6, 17, and 18, showed a much larger binding fractions and were chosen for further analysis. Given the distinct stem-loop structural form of Seq20 in Figure S5, this aptamer was also selected for functional assessment. To confirm the binding abilities of the selected aptamers, the apparent dissociation constants (K_D) were assessed by a fluorescence assay. The binding curves for the six aptamers (seqs 1, 2, 6, 17, 18, and 20) are shown in Figures 2A and S6, and the K_D values of them were found to be at the nM level. The results demonstrate that all of these selected aptamers showed good binding abilities. Particularly, the four aptamers, Seq1, 2, 6, and 18 exhibited the relatively better affinity with

K_D values of (20.4 ± 3.35), (18.2 ± 9.67), (27.1 ± 1.73), and (16.5 ± 5.97) nM, respectively.

Further, truncating strategies were used for the sequence optimization of the selected aptamers, with the consideration of the unnecessary nucleotides and increased synthesis cost for long sequences. We trimmed off external unessential residues of Seq1 at two ends that were not involved in the formation of the stem-loop structure, yielding a 54 nt aptamer, Seq1T. Besides, Seq2T, Seq6T, and Seq18T were generated by using the above truncating strategies. The predicted stem-loop structures of truncated aptamers exhibited almost the same major structure, as shown in Figure S7. This suggests that the middle stem-loop region could be well maintained after truncations. The truncated sequences were chemically synthesized for subsequent characterization. As seen in Figures 2B and S8A–C, all the truncated aptamers displayed lower K_D values as compared with intact sequences, which suggested that they possessed an improved binding performance toward the FAP protein after removing the unnecessary nucleotides. Relevant parameters of biolayer interferometry (BLI) measurements are shown in Figure S9 and Table S5. The results are considered reliable, with mutual authentication by the two methods. The specificities of these aptamers at the protein level are also investigated in Figures 2C and S8D–F. In contrast to target protein FAP, limited binding fractions were observed toward the competing proteins, including glycoproteins [DPP4, ovalbumin (OVA), and transferrin (TRF)] and nonglycoproteins (de-FAP, BSA, and catalase). The three glycoproteins are all N-glycosylated proteins,^{46–48} and DPP4 is also a serine protease similar to FAP. These results indicate that the selected aptamers provide specific binders for the

recognition of the glycosylated FAP protein. Overall, the recognition performances of the four truncated aptamers are satisfactory based on the two aspects of binding ability and selectivity. Among these aptamers, Seq2T was the champion aptamer because of the best property, giving the lowest K_D value of (9.74 ± 1.86) nM by the fluorescence method or (5.69 ± 0.12) nM by the BLI method and satisfying maximum cross-reactivity less than 17%. The cross-activity was estimated by the ratio of the signals of the interfering proteins to that of the target protein.

To determine the preferential recognition of the Seq2T aptamer, we expanded the competition assays. Three common saccharide standards [SA, mannose (Man), and sLeX] were used to assess whether free saccharides could inhibit binding between aptamer and FAP. We found that each of these standards demonstrated little inhibition of binding, indicating that the aptamer does not interact exclusively with these terminal sugar residues. We also confirmed that the aptamer had only weak interaction with A2G2S2 glycan and high mannose glycans, which were obtained through digestion from the glycoprotein TRF and RNase B,^{46,47} while a large decrease was observed when using glycans from FAP in the competition assay. This result suggests that the aptamer does not simply bind any polysaccharide but rather recognizes glycans from FAP. We were unable to determine the exact nature of aptamer-FAP recognition due to the many different types of *N*-glycans present on FAP. It is possible that the aptamer does not recognize a single glycan but rather forms simultaneous contacts with multiple glycans present on FAP. In addition, the inhibition level ($\sim 54\%$ reduction) by glycans from FAP is obviously lower than free FAP, demonstrating that the aptamer has stronger affinity toward glycosylated FAP protein. There could be many reasons for this. For example, the aptamer may form some interactions with protein epitopes, or it is probably due to the different conformational states of solution-phase and protein-linked *N*-glycans.

We also checked the sequences using the Quadruplex-forming G Rich Sequences (QGRS) Mapper website (Table S6). The higher G-Score that evaluates a QGRS for its likelihood to form a stable G-quadruplex indicated these aptamers were better candidates for G-quadruplexes. By incorporating G-quadruplex formation into the structure prediction algorithm, the minimum free energy (dG) values of truncated aptamers demonstrated a significant reduction, indicating the better stability in the G-quadruplex form (Figure 3A–C). To test whether they contained G-quadruplex structures, we carried out the thioflavin (THT) fluorescence experiment, which is known about the enhancement of the G-quadruplex on the fluorescence of THT.⁴⁹ PW-17 was a 17-mer G-rich oligomer for positive control, whereas the randomized sequence (Ran, 54-mer) was negative control. As shown in Figure S10, the four truncated aptamers (Seq1T, 2T, 6T, and Seq18T) dramatically enhanced the fluorescence intensity of THT, and the enhancement coefficient is approximately 35–50 times that of the THT. Circular dichroism (CD) analysis further confirmed these truncated aptamers forming the parallel G-quadruplexes as it generated the CD signals at approximately 240 and 260 nm.⁵⁰

Molecular Docking. To reveal the possible binding region between the aptamer and FAP, we performed molecular docking analysis. The tertiary structure of the aptamer was simulated (see Supporting Information for the procedures), and the structure of FAP was retrieved from the RCSB PDB

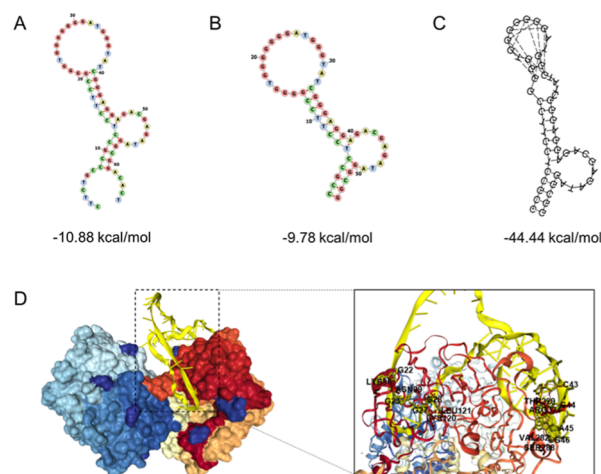


Figure 3. Predicted secondary structures of (A) Seq2 and (B) Seq2T. (C) Predicted secondary structures of Seq2T incorporating G-quadruplex formation into the structure prediction algorithm. (D) Molecular docking model of Seq2T with FAP proteins and details of the binding sites.

data bank (ID: 1Z68). Molecular docking simulations were performed using the HDOCK web service, and the optimal docking model was selected based on the docking score. After the docking analysis, the interactions between the aptamer and the FAP protein in complexes were observed, which indicated possible binding regions. As shown in Figure 3D, LYS96, ASN99, LYS120, LEU121, VAL282, SER288, ARG324, and THR329 of FAP and G22, G23, G27, C28, C43, G44, A45, and G46 of Seq2T mainly participate in the interactions. These residues are close to the glycosylation sites of FAP (ASN92 site and ASN314 site) according to the UniProt database that FAP has five potential N-linked glycosylation sites on asparagine residues: 49, 92, 227, 314, and 679. The docking analysis of other truncated sequences also demonstrated similar residue regions closing the glycosylation sites (Figure S11). Due to unknown structures of the glycans and the difficulty in glycan-involved simulations, the simulations did not consider the involvement of the glycans so that the real situation may be different from the simulations. Even so, the results of binding residue regions around FAP glycosylation sites indicate that the *in vitro* aptamer screening was successful.

Development of the FAP Sensor Based on *oda*-PISA.

By integrating the champion glycan-binding aptamer Seq2T and ultrasensitive SERS detection technology, we developed a rapid FAP detection strategy by constructing an orthogonal dual aptamer (*oda*)-based PISA. The principle of this strategy and the procedure of the *oda*-PISA approach are illustrated in Figure 4A. The champion aptamer Seq2T was immobilized onto a gold thinlayer-coated substrate through the formation of the S–Au bond, followed by capturing FAP protein in the samples. Further, the captured protein was labeled with A1 aptamer-modified silver-based Raman-active nanotags, forming sandwich-like complexes on the substrates. The A1 aptamer was a FAP whole protein-binding aptamer, and it has been described in the recent literature,⁵¹ giving a K_D value of about 500 nM. Upon being shined with a laser beam, the gold-based substrate generated surface plasmon, which excited the silver-based Raman nanotags to generate the plasmon-enhanced Raman scattering signal.

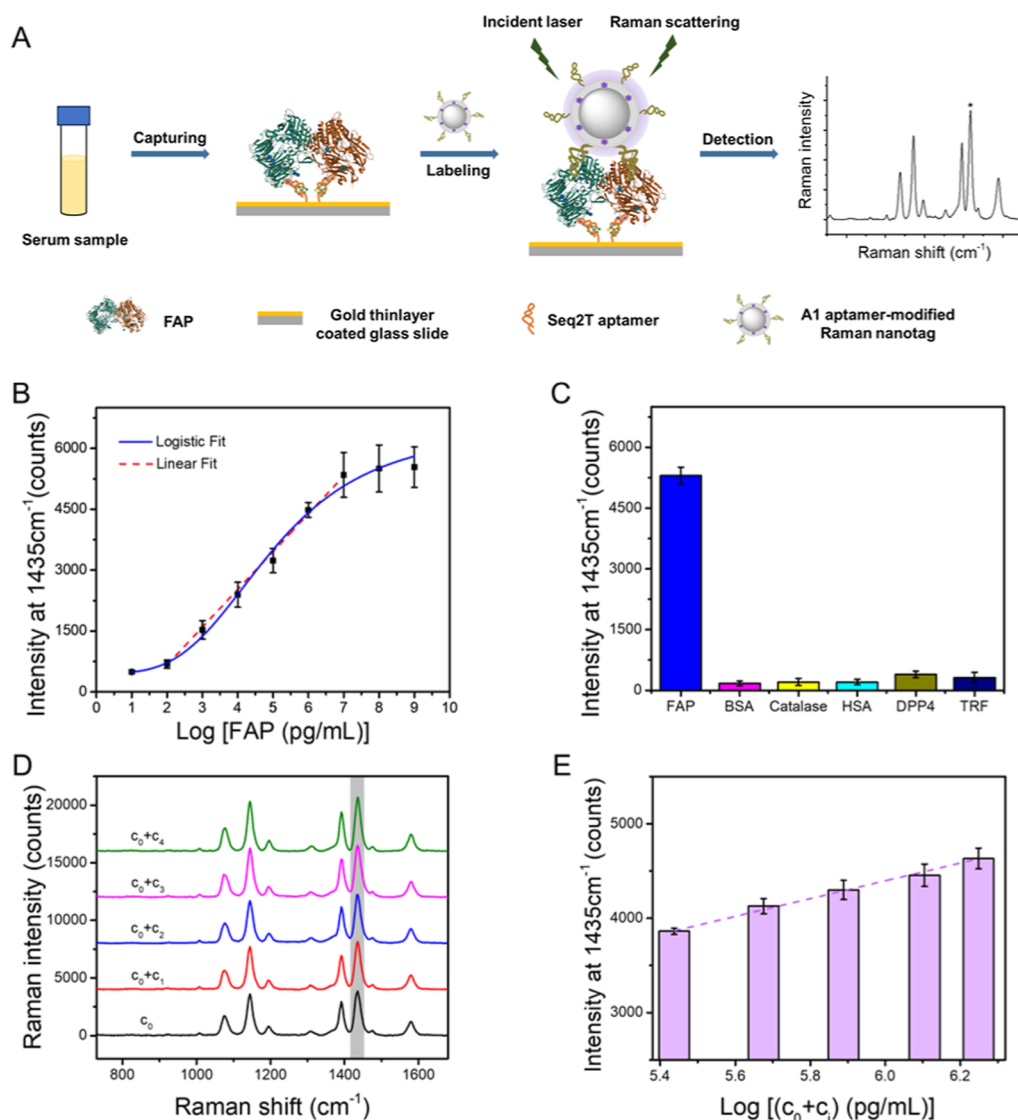


Figure 4. (A) Illustration of the principle of the FAP sensor based on oda-PISA. (B) Dependence of the Raman intensity of oda-PISA on the different concentration of FAP. Linear relationship: $y = -1197.20 + 930.67x$, $R^2 = 0.997$. (C) Selectivity of oda-PISA toward different proteins. (D) Raman spectra for gallbladder cancer patient serum samples spiked with known concentrations of FAP (the spiked concentration for c_1 to c_4 were 200, 500, 1000, and 1500 ng/mL, respectively) and (E) linear relationship between the Raman intensity and the logarithm of the total concentration of FAP ($c_0 + c_i$) in serum samples of the gallbladder cancer patient ($y = -1250.96 + 941.16x$, $R^2 = 0.995$). The error bars represent the standard deviation for three parallel experiments.

In this study, a gold thinlayer-coated glass slide (25×10 mm) with three-spot (1×3) arrays was employed as the substrate (Figure S12), which can be facily fabricated into any desired format with larger numbers of spots for high-throughput assays. A1 aptamer-modified silver-based Raman-active nanotags were prepared as a previous work³⁵ with slight modifications using the synthetic route described in Figure S13A. The average diameters of bare AgNPs and aptamer-modified silver-based Raman nanotags were about 60 and 80 nm, respectively (Figure S13B–D). The UV–vis absorption spectra and Raman spectra of related NPs in the preparation process of A1 aptamer-modified Ag/PATP@SiO₂ NPs nanotags are shown in Figure S13E,F. The appearance of Raman peaks indicates that *p*-amino-thiophenol (PATP) was successfully modified, and the characteristic peak at 1435 cm^{-1} was employed in later oda-PISA assays for quantitative detection.

To verify the successful modification of the aptamer on Ag/PATP@SiO₂ NPs or gold thinlayer-coated glass slide array, the

Raman spectra for oda-PISA of FAP on different combination modes were compared in Figure S13G. The result suggests that a strong Raman signal could be generated only when both aptamers were successfully modified. In addition, we observed that the detection signal of the oda-PISA sensor was apparently reduced if we reversed the order of the A1 aptamer and Seq2T (Figure S14), suggesting that Seq2T is more suitable as a capture receptor due to its satisfied affinity property. Therefore, the mode of A1 aptamer-modified nanotags combined with the Seq2T aptamer-modified array generated a much stronger signal effect.

Linear Response Range and Selectivity of oda-PISA.

The target-concentration-dependent response of oda-PISA was examined by plotting the Raman intensities at 1435 cm^{-1} against the logarithm of the FAP concentration. As shown in Figure 4B, the signal gradually increased with an increasing target concentration. Via fitting the data by the logistical function, the overall K_D value was estimated to be 1.08 nM (R^2

= 0.998). The dependence of intensity on the logarithm of concentration was linear within the range of 100 pg/mL–10 μ g/mL ($y = -1197.20 + 930.67x$, $R^2 = 0.997$), and the linear relationship was used as a calibration curve for further serum sample quantitative analysis. The limit of detection and limit of quantitation (LOQ) of the approach were 10 and 100 pg/mL ($S/N = 10$), which is obviously superior to the level of previous literatures,^{52,53} suggesting that odA-PISA exhibited ultrahigh sensitivity. In order to investigate the selectivity of the developed odA-PISA approach, FAP and five interfering proteins were used as test proteins. Human serum albumin is chosen because it is a high-abundance interfering protein in the blood. As shown in Figures 4C and S15, the interfering proteins exhibited much lower Raman signal intensity as compared with FAP, even presenting at much more stringent conditions (10-fold higher) than that for the target. The cross-activity was within 3.3–7.4%, which had a significant selectivity improvement by comparison with that of individual aptamer Seq2T (Figure 2C). This result indicates that odA-PISA had an excellent specificity toward the target protein, and it can be attributed to the dual selectivity of the aptamer pair.

Detection of FAP in Human Serum Samples. A soluble form of FAP as a minimally invasive serology marker of disease is highly attractive, and distinct FAP expressions have been defined in different biological processes.^{54–56} Herein, the serum FAP levels of healthy individuals and cancer patients were measured with the developed odA-PISA approach. According to the linear calibration curve (Figure 4B), the serum FAP concentration (c_0) of a gallbladder cancer patient (P1) was calculated to be 273.81 ± 22.62 ng/mL. These results were verified through the standard addition method with the assumption that the matrix effect could be effectively eliminated in our assays. The serum samples were spiked with the FAP standard solution with known concentrations (c_i), and then, they were measured by the odA-PISA approach. The Raman spectra for the spiked serum samples from the gallbladder cancer patient are shown in Figure 4D. We further plotted the Raman intensities at 1435 cm^{-1} against the logarithm of total FAP concentrations ($c_0 + c_i$), and we conducted the linear fitting (Figure 4E). The obtained plot obeyed a good linear relationship, which was very close to the calibration curve. So, the assumption was verified to be reasonable, and the initially calculated concentration for the unspiked sample can be considered as the test results. Similarly, the serum FAP level of a healthy individual (H1) was measured to be 98.29 ± 9.59 ng/mL and verified through the standard addition method (Figure S16). Reproducibility assays were also conducted with serum sample H1 using five different stocks of arrays and Raman nanotags (Table S7), indicating good reproducibility of the method. For comparison, enzyme-linked immunosorbent assays (ELISA) of the same serum samples were also carried out using a commercial kit, and the linear calibration curve for the ELISA is shown in Figure S17A. The concentrations of FAP in serum samples of three healthy individuals (H1–H3) and eight cancer patients (P1–P8) by ELISA and the current method were detected in Figure S17B and Table S8. The results by the two methods were found to be consistent with each other, indicating the reliability and feasibility of the current method for real sample application. Given the fast and sensitive response as well as a wide detection range, our method is more cost-efficient and obviates tedious sample pretests.

CONCLUSIONS

In summary, we have successfully developed FAP glycan-targeted aptamers through a rigid glycan-guided screening process. After structural optimization and comprehensive evaluation, four truncated aptamers demonstrated a satisfied affinity and specificity. The champion aptamer seq2T gave the lowest apparent dissociation constant value at 9.74 nM and maximum cross-reactivity of less than 17%. The aptamer developed in this study rivals the binding affinity of the commonly used anti-FAP antibodies (sibrotuzumab, ESC11, and ESC14), which typically exhibit a few nanomolar levels (1–5 nM reported by Renner and co-workers⁵⁷). Regarding the relatively weak noncovalent binding interactions between sugars and oligonucleotides, the generated aptamer seq2T demonstrated a generally acceptable result.

Further, integrating with ultrasensitive SERS detection technology, we established a high-performance dual aptamer-based sandwich sensor. The combined use of the selected glycan-targeting aptamer and protein-binding aptamer apparently improved the detectability of FAP with an LOQ at 100 pg/mL and a maximum cross-reactivity less than 8%. By comparison with a commercial kit, this method demonstrated consistent and reliable applications in serum samples. The generation of the glycosylation-targeted aptamer played essential roles in this approach, (i) considering the significant biological functions of glycosylation in FAP structural stability and endopeptidase activity, the FAP glycan-targeted aptamers can serve not only as available recognition tools in detection devices but also as potential inhibitors in the therapeutic field. (ii) The glycan-binding aptamers could greatly lessen the labor of picking orthogonal aptamer pairs in sandwich assays because of the certain binding sites at the glycan region. Thus, this method is advantageous and opens an exciting avenue to the construction of specific and sensitive FAP detection assays for pan-tumoral diagnosis.

ASSOCIATED CONTENT

Supporting Information

The Supporting Information is available free of charge at <https://pubs.acs.org/doi/10.1021/acs.analchem.4c03770>.

Experimental details, including reagents and chemicals, instruments, preparation of amino-functionalized MNPs, immobilization of target, PCR amplification, ssDNA production and next-generation sequencing, monitoring the selection process, characterization of the candidate aptamers, G-quadruplex structure confirmation, molecular docking, preparation of aptamer-modified array, preparation of Raman nanotags, absorption isotherm and binding constant measurement, cross-reactivity test for PISA, quantitative detection of serum FAP in healthy people and cancer patient, and commercial kit-based ELISA (PDF)

AUTHOR INFORMATION

Corresponding Author

Wei Li – School of Basic Medical Sciences, Zhengzhou University, Zhengzhou 450001, China; orcid.org/0000-0002-2047-2166; Email: liwei_dzlisha@zzu.edu.cn

Authors

Junyang Chen – School of Life Sciences, Zhengzhou University, Zhengzhou 450001, China

Pengfei Ma – The First Affiliated Hospital of Zhengzhou University, Zhengzhou 450001, China

Jiayu Xu – School of Basic Medical Sciences, Zhengzhou University, Zhengzhou 450001, China

Mingxi Zang – School of Basic Medical Sciences, Zhengzhou University, Zhengzhou 450001, China

Complete contact information is available at:

<https://pubs.acs.org/10.1021/acs.analchem.4c03770>

Author Contributions

All authors have given approval to the final version of the manuscript.

Notes

The authors declare no competing financial interest.

ACKNOWLEDGMENTS

We acknowledge the funding support from the National Natural Science Foundation of China (22304166), the Qushi Scientific Research Program of Zhengzhou University (32213131), and the Henan Provincial Science and Technology Research Project (242102311139).

REFERENCES

- (1) Siegel, R. L.; Giaquinto, A. N.; Jemal, A. *Ca-Cancer J. Clin.* **2024**, *74*, 12–49.
- (2) Hinshaw, D. C.; Shevde, L. A. *Cancer Res.* **2019**, *79*, 4557–4566.
- (3) Joshi, R. S.; Kanugula, S. S.; Sudhir, S.; Pereira, M. P.; Jain, S.; Aghi, M. K. *Cancers* **2021**, *13*, 1399.
- (4) Nurmik, M.; Ullmann, P.; Rodriguez, F.; Haan, S.; Letellier, E. *Int. J. Cancer* **2020**, *146*, 895–905.
- (5) Lindner, T.; Loktev, A.; Giesel, F.; Kratochwil, C.; Altmann, A.; Haberkorn, U. *EJNMMI Radiopharm. Chem.* **2019**, *4*, 16.
- (6) Fitzgerald, A. A.; Weiner, L. M. *Cancer Metastasis Rev.* **2020**, *39*, 783–803.
- (7) Zi, F. M.; He, J. S.; He, D. H.; Li, Y.; Yang, L.; Cai, Z. *Mol. Med. Rep.* **2015**, *11*, 3203–3211.
- (8) Lee, K. N.; Jackson, K. W.; Christiansen, V. J.; Lee, C. S.; Chun, J. G.; McKee, P. A. *Blood* **2006**, *107*, 1397–1404.
- (9) Chen, W. T.; Kelly, T.; Ghersi, G. *Curr. Top. Dev. Biol.* **2003**, *54*, 207–232.
- (10) Aggarwal, S.; Brennen, W. N.; Kole, T. P.; Schneider, E.; Topaloglu, O.; Yates, M.; Cotter, R. J.; Denmeade, S. R. *Biochemistry* **2008**, *47*, 1076–1086.
- (11) Lin, Y.; Ma, Z.; Li, Z.; Gao, Y.; Qin, X.; Zhang, Z.; Wang, G.; Du, L. A.-O.; Li, M. A.-O. *Anal. Chem.* **2019**, *91*, 14873–14878.
- (12) Liu, J. Y.; Huang, C. Q.; Peng, C. W.; Xu, F.; Li, Y.; Yutaka, Y.; Xiong, B.; Yang, X. J. *BMC Cancer* **2018**, *18*, 1099.
- (13) Kraman, M.; Bambrough, P. J.; Arnold, J. N.; Roberts, E. W.; Magiera, L.; Jones, J.; Gopinathan, A.; Tuveson, D. A.; Fearon, D. T. *Science* **2010**, *330*, 827–830.
- (14) Ruan, P.; Tao, Z.; Tan, A. *Biosci. Rep.* **2018**, *38*, BSR20171027.
- (15) Edosada, C. Y.; Quan, C.; Tran, T.; Pham, V.; Wiesmann, C.; Fairbrother, W.; Wolf, B. B. *FEBS Lett.* **2006**, *580*, 1581–1586.
- (16) Song, P. F.; Pan, Q. S.; Sun, Z. H.; Zou, L. W.; Yang, L. *Chem.-Biol. Interact.* **2022**, *354*, 109830.
- (17) Li, Y. Q.; Liu, B. W.; Huang, Z. C.; Liu, J. W. *Chem. Sci.* **2020**, *11*, 2735–2743.
- (18) Song, Y. L.; Song, J.; Wei, X. Y.; Huang, M. J.; Sun, M.; Zhu, L.; Lin, B. Q.; Shen, H. C.; Zhu, Z.; Yang, C. Y. *Anal. Chem.* **2020**, *92*, 9895–9900.
- (19) Tuerk, C.; Gold, L. *Science* **1990**, *249*, 505–510.
- (20) Ellington, A. D.; Szostak, J. W. *Nature* **1990**, *346*, 818–822.
- (21) Zhu, C.; Feng, Z. R.; Qin, H. W.; Chen, L.; Yan, M. M.; Li, L. S.; Qu, F. *Talanta* **2024**, *266*, 124998.
- (22) Yang, K.; Mitchell, N. M.; Banerjee, S.; Cheng, Z. Z.; Taylor, S.; Kostic, A. M.; Wong, I.; Sajjath, S.; Zhang, Y. M.; Stevens, J.; Mohan, S.; Landry, D. W.; Worgall, T. S.; Andrews, A. M.; Stojanovic, M. N. *Science* **2023**, *380*, 942–948.
- (23) Zhang, Y.; Lai, B. S.; Juhas, M. *Molecules* **2019**, *24*, 941.
- (24) Ismail, S. I.; Alshaer, W. *Adv. Drug Delivery Rev.* **2018**, *134*, 51–64.
- (25) Gu, F. F.; Sun, M. X.; Zhang, Y.; Xie, J.; Gao, Q. X.; Duan, W. J.; Chen, J. X.; Chen, J.; Dai, Z.; Li, M. M. *Sens. Actuators, B* **2023**, *389*, 133890.
- (26) Zhao, Z. Y.; Yang, S.; Tang, X. Q.; Feng, L.; Ding, Z. S.; Chen, Z. G.; Luo, X.; Deng, R. J.; Sheng, J.; Xie, S.; Chang, K.; Chen, M. *Biosens. Bioelectron.* **2024**, *246*, 115841.
- (27) Minopoli, A.; Della Ventura, B.; Lenyk, B.; Gentile, F.; Tanner, J. A.; Offenhäusser, A.; Mayer, D.; Velotta, R. *Nat. Commun.* **2020**, *11*, 6134.
- (28) Kim, G.; Yang, H. *Biosens. Bioelectron.* **2024**, *253*, 116184.
- (29) Zhao, S. Q.; Huang, J. W.; Li, D. S.; Yang, L. *Biosens. Bioelectron.* **2022**, *214*, 114505.
- (30) Muhammad, M.; Huang, Q. *Talanta* **2021**, *227*, 122188.
- (31) Chen, M. Y.; Xie, Y. C. Z.; Li, M. *Nano Lett.* **2024**, *24*, 11520–11528.
- (32) Zhou, L. L.; Wang, Y. J.; Xing, R. R.; Chen, J.; Liu, J.; Li, W.; Liu, Z. *Biosens. Bioelectron.* **2019**, *145*, 111729.
- (33) Ge, G.; Wen, Y. R.; Li, P. F.; Guo, Z. C.; Liu, Z. *Anal. Chem.* **2023**, *95*, 17502–17512.
- (34) Xing, R. R.; Wen, Y. R.; Dong, Y. R.; Wang, Y. J.; Zhang, Q.; Liu, Z. *Anal. Chem.* **2019**, *91*, 9993–10000.
- (35) Li, W.; Zhang, Q.; Wang, Y. J.; Ma, Y. Y.; Guo, Z. C.; Liu, Z. *Anal. Chem.* **2019**, *91*, 4831–4837.
- (36) Ma, Y. Y.; Li, X. L.; Liu, J.; Li, W.; Liu, Z. *ACS Sens.* **2020**, *5*, 1436–1444.
- (37) Yang, Q.; Jia, C. Z.; Li, T. Y. *Math. Biosci.* **2019**, *311*, 103–108.
- (38) Park, J.-W.; Lee, S. J.; Choi, E.-J.; Kim, J.; Song, J.-Y.; Gu, M. B. *Biosens. Bioelectron.* **2014**, *51*, 324–329.
- (39) Nguyen, T. T. Q.; Kim, E. R.; Gu, M. B. *Biosens. Bioelectron.* **2022**, *198*, 113835.
- (40) Díaz-Fernández, A.; Miranda-Castro, R.; de-los-Santos-Álvarez, N.; Rodríguez, E. F.; Lobo-Castañón, M. J. *Biosens. Bioelectron.* **2019**, *128*, 83–90.
- (41) Díaz-Fernández, A.; Miranda-Castro, R.; Díaz, N.; Suárez, D.; de-los-Santos-Álvarez, N.; Lobo-Castañón, M. J. *Chem. Sci.* **2020**, *11*, 9402–9413.
- (42) Li, W.; Ma, Y. Y.; Guo, Z. C.; Xing, R. R.; Liu, Z. *Anal. Chem.* **2021**, *93*, 956–963.
- (43) Li, W.; Xu, S. X.; Li, Y.; Chen, J. R.; Ma, Y. Y.; Liu, Z. *CCS Chem.* **2023**, *5*, 497–509.
- (44) Yoshikawa, A. M.; Rangel, A.; Feagin, T.; Chun, E. M.; Wan, L.; Li, A.; Moeckl, L.; Wu, D.; Eisenstein, M.; Pitteri, S.; Soh, H. T. *Nat. Commun.* **2021**, *12*, 7106.
- (45) Tommasone, S.; Allabush, F.; Tagger, Y. K.; Norman, J.; Köpf, M.; Tucker, J. H. R.; Mendes, P. M. *Chem. Soc. Rev.* **2019**, *48*, 5488–5505.
- (46) Spik, G.; Bayard, B.; Fournet, B.; Strecker, G.; Bouquelet, S.; Montreuil, J. *FEBS Lett.* **1975**, *50*, 296–299.
- (47) Thaysen-Andersen, M.; Mysling, S.; Højrup, P. *Anal. Chem.* **2009**, *81*, 3933–3943.
- (48) Kawasaki, N.; Lin, C.-W.; Inoue, R.; Khoo, K.-H.; Kawasaki, N.; Ma, B. Y.; Oka, S.; Ishiguro, M.; Sawada, T.; Ishida, H.; Hashimoto, T.; Kawasaki, T. *Glycobiology* **2008**, *19*, 437–450.
- (49) Yang, G. T.; Li, W.; Zhang, S.; Hu, B.; Huang, Z. *Talanta* **2024**, *266*, 125039.
- (50) Okamoto, C.; Momotake, A.; Yamamoto, Y. *J. Inorg. Biochem.* **2021**, *216*, 111336.
- (51) Zhang, X. M.; Yang, G.; Zhao, Y.; Dai, X. Y.; Liu, W. J.; Qu, F.; Huang, Y. Y. *Molecules* **2023**, *28*, 1682.
- (52) Lin, Y. X.; Ma, Z.; Li, Z. Z.; Gao, Y. Q.; Qin, X. J.; Zhang, Z.; Wang, G. K.; Du, L. P.; Li, M. Y. *Anal. Chem.* **2019**, *91*, 14873–14878.
- (53) Fu, A. C.; Wang, H. B.; Huo, T. T.; Li, X. W.; Fu, W.; Huang, R. Q.; Cao, Z. *J. Anal. Chem.* **2021**, *93*, 6501–6507.

- (54) Yazbeck, R.; Jaenisch, S. E.; Abbott, C. A. *Protoplasma* **2018**, *255*, 375–386.
- (55) Uitte de Willige, S.; Malfliet, J. J.; Janssen, H. L.; Leebeek, F. W.; Rijken, D. C. *J. Thromb. Haemostasis* **2013**, *11*, 2029–2036.
- (56) Uitte de Willige, S.; Malfliet, J. J.; Deckers, J. W.; Dippel, D. W.; Leebeek, F. W.; Rijken, D. C. *Int. J. Cardiol.* **2015**, *178*, 105–110.
- (57) Fischer, E.; Chaitanya, K.; Wüest, T.; Wadle, A.; Scott, A. M.; van den Broek, M.; Schibli, R.; Bauer, S.; Renner, C. *Clin. Cancer Res.* **2012**, *18*, 6208–6218.